


Calculating the ground-state energy of benzene under spatial deformations with noisy quantum computing

Wassil Sennane^{1,*}, Jean-Philip Piquemal^{2,†} and Marko J. Rančić^{1,‡}

¹TotalEnergies, Tour Coupole, La Défense, 2 Pl. de la Coupole-Jean Millier, 92400 Courbevoie, France

²Laboratoire de Chimie Théorique, UMR No. 7616, CNRS, Sorbonne Université, 75052 Paris, France

 (Received 8 April 2022; revised 8 November 2022; accepted 16 December 2022; published 11 January 2023)

In this paper we calculate the ground-state energy of benzene under spatial deformations by using the variational quantum eigensolver. The primary goal of the study is to estimate the feasibility of using quantum computing *Ansätze* on near-term devices to solve problems with a large number of orbitals in regions where classical methods are known to fail. Furthermore, by combining our advanced simulation platform with real quantum computers, we provide an analysis of how the noise, inherent to quantum computers, affects the results. At the center of our study are the hardware efficient and quantum unitary coupled-cluster (QUCC) *Ansätze*. First, we find that the hardware efficient *Ansatz* has the potential to outperform mean-field methods for extreme deformations of benzene. However, key problems remain at equilibrium, preventing real chemical application. Moreover, the hardware efficient *Ansatz* yields results that strongly depend on the initial guess of parameters (in both noisy and noiseless cases) and optimization issues have a higher impact on their convergence than noise. This is confirmed by comparison with real quantum computing demonstrations. On the other hand, the QUCC *Ansatz* alternative exhibits deeper circuits. Therefore, noise effects increase and are so extreme that the method never outperform mean-field theories. Our dual simulator, (8–16)-qubit QPU computations of QUCC *Ansatz* appears to be much more sensitive to hardware noise than shot noise, which further indicates where the noise-reduction efforts should be directed. Finally, the study shows that the QUCC method better captures the physics of the system as the QUCC method can be utilized together with the Hückel approximation. We discussed how going beyond this approximation sharply increases the optimization complexity of such a difficult problem.

DOI: [10.1103/PhysRevA.107.012416](https://doi.org/10.1103/PhysRevA.107.012416)

I. INTRODUCTION

Quantum computing has opened a new era of calculations due to quantum superposition and quantum entanglement. While classical computers handle binary information, quantum computers use an entangled superposition of states as information carriers. Some algorithms, such as the well-known Grover algorithm [1] and Shor's algorithm [2], will introduce new efficient ways of solving complex problems if implemented on quantum computers. Moreover, the deepest understanding of complex molecules will become possible [3] with new techniques such as the quantum phase estimation (QPE) algorithm [4,5] and the variational quantum eigensolver (VQE) algorithm [6–15]. This new technology uses very fragile entangled states of matter, which makes the management of multiple qubits without error correction difficult. As QPE requires quantum error correction, we focus solely on the VQE in this paper.

There are in principle two approaches in which quantum computing is foreseen to provide value: through development of quantum inspired algorithms which are executed on quantum simulators and through algorithms which are executed

on actual quantum hardware. Quantum simulators exploit advanced supercomputing platforms to emulate quantum-computing-like environments. On the other hand, a bottleneck in executing algorithms on actual hardware is produced by quantum noise processes: qubit dephasing, qubit relaxation, and readout errors. With two-qubit error rates on the order of 1%, the maximal number of two-qubit gates applied in a circuit is a few hundred [16,17].

An open question remains: Could either of these two approaches offer immediate value in treating problems beyond, for instance, very simple molecules? We try to address these questions by solving the problem of benzene, a cyclic molecule with the formula C_6H_6 .

In order to minimize the number of qubits required for a computation, we choose to work with the least computationally demanding basis: sto-3g. In addition to the computational cost savings, this minimal basis set will amplify the errors, which can help us identify the shortcomings of the methods we use. In this basis, each H is represented with a $1s$ orbital and each C is represented with $1s$, $2s$, $2p_x$, $2p_y$, and $2p_z$ orbitals [18]. Therefore, the treatment of the entire molecule requires taking into account 36 orbitals or equivalently 72 spin orbitals for which 72 qubits would be required. Because simulating 72 qubits is beyond the simulation capabilities of our in-house simulator, which is capable of simulating up to 35 qubits, our approach relies on a reduction of the size of the system via active-space selection. Then 132 qubits would

*wassil.sennane@totalenergies.com

†jean-philip.piquemal@sorbonne-universite.fr

‡marko.rancic@totalenergies.com

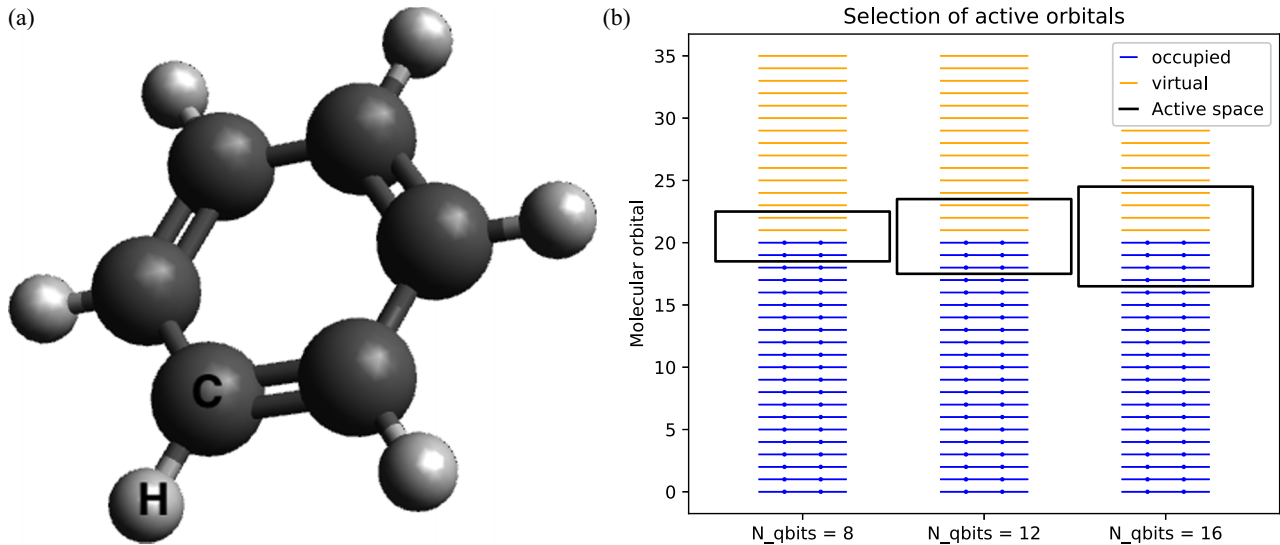


FIG. 1. (a) Molecular geometry of benzene. (b) Selections of the active orbital space used throughout the paper.

be required with the 6-31g basis and 228 qubits with the cc-pVDZ basis set.

In this paper we consider four ways of selecting the active orbital case. Figure 1(b) shows the active spaces used in this paper, all of which have an equal number of occupied and virtual orbitals. Intensive numerical testing shows that those active spaces with N electrons on N orbitals lead to lower energies as opposed to active spaces with unequal numbers of occupied and virtual orbitals.

In order to test the added value of contemporary quantum computing methodologies, we focus on situations where mean-field theories such as Hartree-Fock and density-functional theories are not precise enough [19,20]. Furthermore, we search for situations where classical coupled-cluster *Ansätze* are expected to yield nonphysical solutions and full configuration-interaction calculations are, although theoretically possible, quite impractical due to a large active space [20,21]. Such situations occur when systems with a large number of orbitals are subject to spatial deformations, referred to as distortions. We choose three types of such distortions. For each of these distortions, we compute the Hamiltonian of the molecule in the three cases described in Fig. 1(b) and calculate their lowest eigenvalue, which corresponds to the ground-state energy of the size-reduced system.

Figure 2 describes the three types of distortions we use in this paper. All the distortions studied here have the same spacing between one carbon and its closest neighboring hydrogen atom. This distance is fixed at 1.09 Å as in the equilibrium conformation of benzene. Generally, all fixed parameters have their equilibrium value. The first distortion is a uniform deformation of the molecule, in which the distance between two neighboring carbon atoms R_1 varies. In the second distortion, as Fig. 2 shows, the variable parameter is the distance R_2 between two opposite sides of the hexagon. The distance between the carbon atoms on each of these sides does not vary. Moreover, the two carbon atoms not on one of these sides have their spacing fixed. During the distortion, these two carbon atoms are vertically halfway between the two sides. For the third distortion, the idea is to divide the benzene into

two identical triplets of carbon-hydrogen pairs. Then these two parts are laterally moved one from another by varying the parameter R_3 .

TotalEnergies is in possession of a quantum learning machine (QLM) [22], which allows large-scale simulations of quantum processing units (QPUs). This platform, operating 192 cores and 3 TB of RAM, is also compatible with QPUs from various providers such as IBM's quantum computers. In particular, the IBMQ_Toronto quantum processing unit has T_1 and T_2 approximately at 100 μ s, with an average controlled-NOT (CNOT) error rate about 10^{-2} . Moreover, it should be noted that both MYQLM, an open source version of the QLM libraries used, and the codes for this study are public [23].

This paper is organized as follows. In Sec. II we describe the methodology. In Sec. III we show and discuss all our simulations with an increasing level of complexity, going from noiseless simulations to compare different *Ansätze* and identify optimizations issues, introducing shot noise, and finally comparing simulated noise to real demonstrations in IBMQ. We summarize in Sec. IV.

II. METHODS

A. State-of-the-art classical computing methodologies

A number of classical computational chemistry methods were performed in order to benchmark the quantum computing results: Hartree-Fock (HF), second-order Møller-Plesset perturbation theory (MP2), coupled-cluster single and double (CCSD) and triple (CCSDT), configuration interaction with single and double excitations (CISD), and configuration interaction using a perturbative selection (CIPSI). With these classical methodologies, the benzene system in the sto-3g basis can be treated without orbital freezing. There are many possible open-source realizations for the listed methods. In our case for the HF, MP2, CCSD, CCSDT, and CISD methods, the PYSCF package version 1.7.5.1 was used [24,25] on TotalEnergies in-house high-performance-computing (HPC) architecture. Otherwise, the CIPSI method is the current state-of-the-art methodology for calculating energy levels of

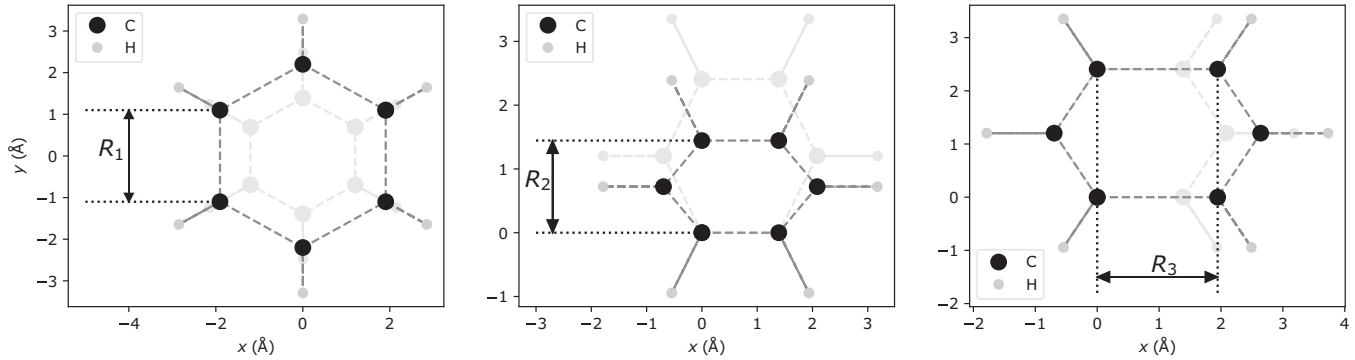


FIG. 2. The three types of distortions studied. In the remainder of the paper these distortions are referred to as distortion 1, distortion 2, and distortion 3 respectively.

benzene [26]. It is implemented in QUANTUM PACKAGE in the Master clusters at the Laboratoire de Chimie Théorique (LCT). An open source implementation of wave-function quantum chemistry methods was used [27], mainly developed at the Laboratoire de Chimie et Physique Quantiques in Toulouse, France, and LCT in Paris. The CIPSI codes were executed in an efficient parallel fashion.

B. Orbital freezing

Chemically, the lowest orbitals will be frozen and considered as full and they will be taken into consideration in the core energy, while the highest orbitals will be considered as nonactive and empty. As Hückel's approximation suggests [28], most of the electronic behavior of aromatic molecules such as benzene is described with the π orbitals of the carbon atoms, so we try to keep them active while reducing the active space. Since the two highest occupied orbitals are degenerate in benzene, the smallest case we consider is four electrons in four orbitals, which corresponds to the eight-qubit case in Fig. 1(b). The 12-qubit case considers all π orbitals active, while our 16-qubit case goes beyond the Hückel approximation. Mathematically, our in-house simulator, the quantum learning machine (QLM) [22], defines two subspaces of indices corresponding to active orbitals \mathcal{A} and occupied orbitals \mathcal{O} . By computing the eigenvalues of the reduced density matrix of the molecule, we obtain the natural orbital occupation numbers n_i for each molecular orbital i of the whole system. Then the two subspaces are filled by a built-in function of the QLM which requires upper and lower thresholds ϵ_1 and ϵ_2 to select the orbitals

$$\begin{aligned} \mathcal{A} &= \{i \mid n_i \in [\epsilon_2, 2 - \epsilon_1]\} \cup \{i \mid n_i \geq 2 - \epsilon_1, 2(i + 1) \\ &\geq N_{\text{elec}}\}, \\ \mathcal{O} &= \{i \mid n_i \geq 2 - \epsilon_1, 2(i + 1) < N_{\text{elec}}\}. \end{aligned} \quad (1)$$

Once we have these subspaces, the built-in function performs an update of the one-body term and the core energy

$$\begin{aligned} h_{pq} &\rightarrow h_{pq} + \sum_{i \in \mathcal{O}} 2h_{ipqi} - h_{ipq} \forall p, q \in \mathcal{A}, \\ E_{\text{core}} &\rightarrow E_{\text{core}} + \sum_{i \in \mathcal{O}} h_{ii} + \sum_{i, j \in \mathcal{O}} 2h_{ijji} - h_{ijij}. \end{aligned} \quad (2)$$

Finally, the choice of the thresholds implies directly the choice of the active orbitals.

C. Variational quantum eigensolver

The VQE [6–15] algorithm gives an estimation of the lowest eigenvalue of an eigenproblem, based on an optimization loop. First, one starts with a molecule, whose one-body and two-body terms are calculated by a chemistry package such as PYSCF [24]. Second, one applies a qubit-mapping transformation, such as the Jordan-Wigner transformation (see Appendix B), in order to obtain H_{JW} . This new Hamiltonian is written as a sum of Pauli strings, so it is understandable and measurable by quantum computers. Third, one creates a unitary state $|\psi(\theta)\rangle$ which depends on a set of parameters and then one computes

$$E(\theta) = \frac{\langle \psi(\theta) | H_{\text{JW}} | \psi(\theta) \rangle}{\langle \psi(\theta) | \psi(\theta) \rangle} = \sum_j h_j \langle \psi(\theta) | P_j | \psi(\theta) \rangle, \quad (3)$$

where P_j are tensor products of Pauli matrices (labeled as Pauli strings in Appendix B) and h_j are weights obtained from the Jordan-Wigner transformation. The result is then communicated to a classical computer, which returns a new set of parameters, so an expectation value of energy of the new trial state $|\psi(\theta')\rangle$ will be calculated again with the quantum computer. This loop occurs until the optimizer finds the minimum energy. Due to the Ritz variational principle, the variational solution obtained by the quantum computer cannot be lower than the exact energy E_0 :

$$E_0 \leq E(\theta) = \langle \psi(\theta) | H_{\text{JW}} | \psi(\theta) \rangle \forall \theta. \quad (4)$$

In the remainder of this paper, a constrained optimization by linear approximation (COBYLA) optimizer with maximally 1000 iterations will be used [29].

A critical point in solving the eigenvalue problem with the VQE is the selection of the trial state. There are mainly two different types of trial states, known as hardware efficient (HE) *Ansätze* and the quantum unitary coupled-cluster (QUCC) *Ansatz*. The QUCC *Ansatz* is a chemically inspired trial state, with a large number of quantum gates and a precise estimation of the ground-state energy [30–33]. The HE *Ansatz* is a trial state designed to be easily implementable on quantum computers [30,34–37] but with a less precise estimation of the ground-state energy.

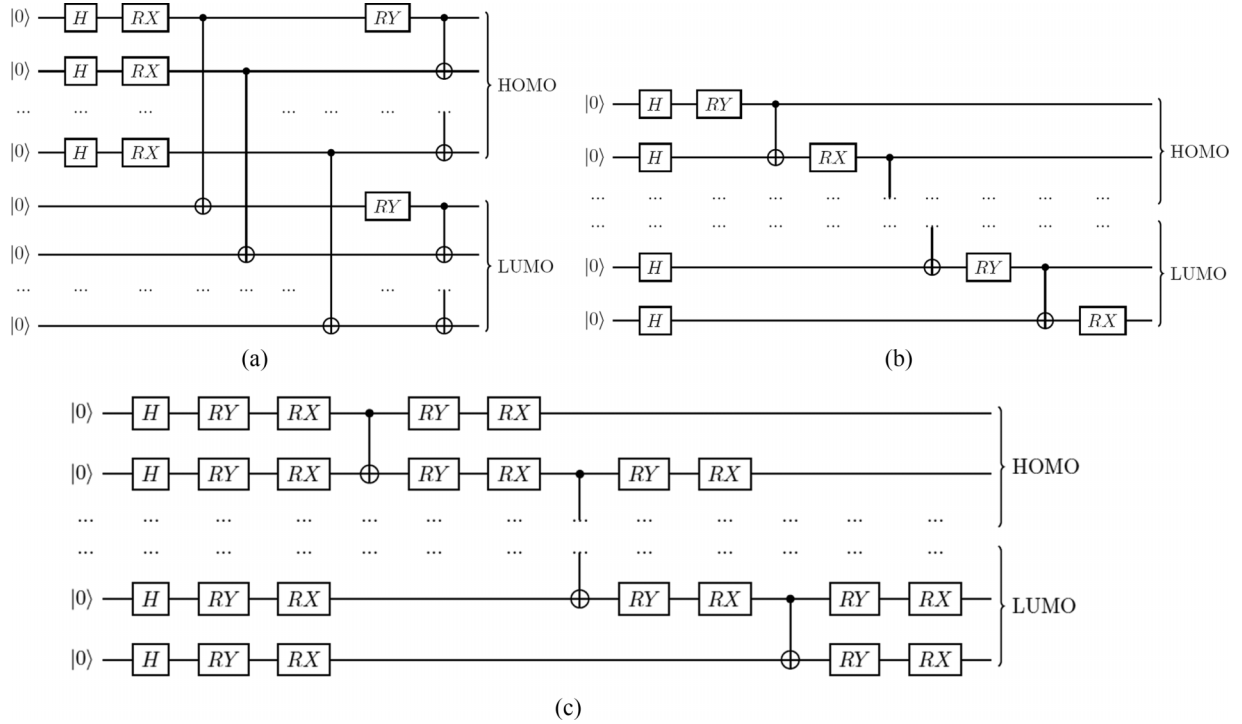


FIG. 3. Hardware efficient circuits used in this study: (a) v1, (b) v2, and (c) v3. All of the RY and RX gates are parametrized by an angle θ . Here the three circuits have their depth $d = 1$. The number of parameters is (a) and (b) dN_{qubits} and (c) $2d(3N_{\text{qubits}} - 2)$.

The Hadamard gate is an integral part of the HE *Ansatz*, enabling the creation of superimposed states. Another ingredient of the HE *Ansatz* is the CNOT gate, a controlled operation which flips the $|0\rangle$ and $|1\rangle$ states if the controlled qubit is $|1\rangle$. The RX and RY gates are the unitary rotation operators around the x and y axes in the Bloch sphere, parametrized by an angle. Defined by the exponentiation of the X and Y Pauli matrices, with these two operators, one is able to cover the whole Bloch sphere [38].

The circuit in Fig. 3(a) is chemically inspired. If we suppose that the first $N_{\text{qubits}}/2$ qubits represent the occupied orbitals, then the Hadamard gate creates an electron on each of them. Starting from this hypothesis, combining these gates with the first set of CNOT entanglements makes an occupied-virtual mixing and then the second set makes a spin mixing. The RX and RY gates parametrize the circuit. The circuit in Fig. 3(b) is a circuit which is easily implementable on a quantum computer with nearest-neighbor two-qubit interactions (a linear chain of qubits). An electron is created in all the orbitals and we use alternatively an RY or an RX gate to parametrize the occupancy of each qubit (orbital). The circuit in Fig. 3(c) is also connectivity inspired with more single-qubit gates compared to its counterpart in Fig. 3(b). We first create an electron on each orbital with the Hadamard gates. Then, knowing that the Hadamard gate is given by a product of RY and RX gates $H = RY(-\frac{\pi}{2})RX(\pi)$, the set of RY - RX gates directly weights the occupancy of each orbital. The CNOT entanglements produce a linear circuit, and after each entanglement we add a new set of RY - RX gates in order to prevent the errors due to noncommuting gates. In other words, this theoretically could enable the circuit to determine

the best order of gates at a cost of an optimization function with a larger number of variational parameters.

In our case, the depth of the circuit is the number of parametrized layers one adds to the first set of Hadamard gates. In Fig. 3 the depth is equal to 1 and the circuits are displayed in the case of a four-qubit Hamiltonian.

For the implementation of the QUCC *Ansatz*, the circuit is provided by built-in functions of the QLM. As an input one- and two-body integrals are required, along with the total number of electrons, the subspace of spin orbitals \mathcal{O} , and the natural orbital occupation numbers and the energies of the active orbitals. By computing $n_{e_{\text{act}}} = n_e - 2|\mathcal{O}|$, one has the number of active electrons, that is to say, the number of electrons that are distributed over the active orbitals. Then \mathcal{A} is divided into two subspaces, \mathcal{I}' , which contains the unoccupied active orbitals, and \mathcal{O}' , which contains the occupied active orbitals, and the anti-Hermitian operator is created,

$$\begin{aligned}
 T_{\text{QUCC}}(\boldsymbol{\theta}) = & \sum_{pr} \theta_p^r (a_p^\dagger a_r - a_r^\dagger a_p) \\
 & + \sum_{p>q, r>s} \theta_{pq}^{rs} (a_p^\dagger a_q^\dagger a_r a_s - a_r^\dagger a_s^\dagger a_p a_q) \\
 & \times \forall p, q, r, s \in \mathcal{I}'^2 \times \mathcal{O}'^2, \quad (5)
 \end{aligned}$$

where $\boldsymbol{\theta}$ is an array of parameters. After that, the built-in functions give the *Ansatz* $|\psi(\boldsymbol{\theta})\rangle = e^{T_{\text{QUCC}}(\boldsymbol{\theta})}|\Phi_0\rangle$, with $|\Phi_0\rangle$ the state obtained with the Hartree-Fock method [22]. The operator is Trotterized up to first order [22,39], which gives Pauli strings that are decomposed in single- and two-qubit gates. Although the initial state would be the Hartree-Fock guess if $\boldsymbol{\theta}_0 = 0$, the QLM calculates an improved $\boldsymbol{\theta}_0$, which

returns the MP2 method guess as the initial guess,

$$\theta_p^r = 0 \forall p, r \in \mathcal{T}' \times \mathcal{O}',$$

$$\theta_{pq}^{rs} = \frac{h_{pqrs} - h_{pqsr}}{\varepsilon_r + \varepsilon_s - \varepsilon_p + \varepsilon_q} \forall p, q, r, s \in \mathcal{T}'^2 \times \mathcal{O}'^2, \quad (6)$$

with ε_i the energy of the orbital i . As the MP2 method is a post-Hartree-Fock method, which takes into account some of the electronic correlation, the initial guess of the QUCC Ansatz is expected to be better.

D. Noise models

In this paper we compute both noiseless and noisy simulations. The noisy simulations take into consideration two types of noise: shot noise and idle hardware noise. Shot noise originates from the final measurement of the qubit register. As we use a simulator of quantum computers, entire circuits are applied to the qubit register and then the machine has access to the exact frequencies. Including shot noise means using a number of random shots to make an estimation of these frequencies and using them as a result. If one wants to measure the exact probabilities of any quantum state, an infinite number of shots is required. In a realistic demonstration it is impossible to perform an infinite number of evaluations. Shot noise is the difference in measured probabilities between a finite and an infinite number of realizations in any demonstrations in quantum computing. Our simulator is able to calculate these two cases by fixing the number of shots n_{shots} , which has to be 0 to obtain the exact probabilities.

The hardware noise describes the decoherence through the execution of the circuit [40–42]. Within our in-house simulator, two ways of incorporating noise exist: an idle noise model and a full noise model. In the first one, the qubit gates are

ideal and the noise appears only when the qubit is inactive. In the latter noise model, decoherence and relaxation occur both when the qubit is actively operated on and when the qubit is inactive. Due to the long simulation times of the full noise model, in the remainder of this paper we will tackle noise from an idle perspective.

Indeed, unlike pure quantum states which are well described with a state vector, open quantum systems must employ a density-matrix description to capture the full noise dynamics. Giving a description of noise in an open quantum system where the state of the environment at time t_1 is correlated with the state of the environment at time $t_2 > t_1$ usually requires a solution of a generalized master equation for the density matrix such as the Zwanzig-Nakajima equation [43,44]. As this integro-differential equation is *per se* unsolvable for a realistic system, further approximations needs to be made such as the commonly employed Markov approximation. The Markov approximation assumes a memoryless environment, one where the state of the environment at time t_1 is totally uncorrelated with the state of the environment at time t_2 . Contemporary quantum computers, such as those from IBM Quantum, have a so-called $1/f$ noise spectral density, where the noise is a mixture of predominantly non-Markovian and a smaller fraction of Markovian noise [45,46]. However, the Lindblad-like equation [47], which is the result of such approximations, is a matrix partial differential equation and is still difficult to solve for large systems. Consequently, our in-house simulator offers simplified quantum noise models.

The QLM allows the incorporation of this model by applying amplitude damping and pure dephasing, with built-in functions which are returned by the noisy quantum processing unit simulator. By manipulating the density matrix describing the qubits with Kraus operators, the dephasing is implemented

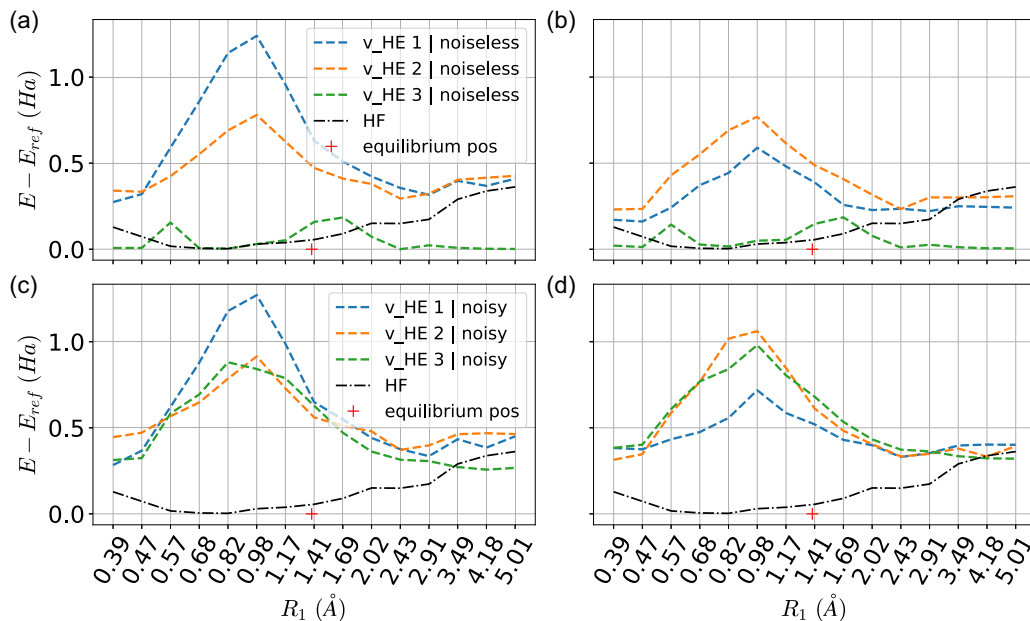


FIG. 4. Difference between the ground-state energy curves of the eight-qubit system obtained with the HE Ansatz and the reference obtained with full diagonalization of the eight-qubit system. All the figures have the same y axis. (a) and (c) $d = 1$, (b) and (d) $d = 2$, (a) and (b) noiseless, and (c) and (d) noisy.

TABLE I. Relaxation, dephasing, and gate-duration times.

T_1	T_2	Z	X	Y	RX	RY	RZ	CNOT
50 μ s	50 μ s	60 ns	60 ns	60 ns	60 ns	60 ns	60 ns	150 ns

with a characteristic decay law on its antidiagonal terms, while the amplitude damping affects both the diagonal and the antidiagonal terms with a similar decay law (see Appendix 3). The built-in functions of the QLM require T_1 and T_2 , the two characteristic relaxation and dephasing times, along with gate duration. Table I lists the values we use in the remainder of the paper.

III. RESULTS

A. Comparison of the HE *Ansätze*

In this section we perform a comparison between the different HE circuits, for size-reduced cases with four electrons in four orbitals and for all three distortions. The first distortion is represented in Fig. 4 (see Fig. 5 for second and third distortions). First, for depths equal to 1 and 2, we display noiseless simulations and then we display noisy simulations. These noisy simulations take into consideration shot noise and an idle noise model of the quantum processing unit. Moreover, while state-of-the-art post-Hartree-Fock solvers such as the CCSD method are known to be very precise around the equilibrium position, they yield nonphysical solutions when the chemical system is distorted [20]. Because of this and the fact that we want to make sure how much two-body correlation quantum computing captures, we choose the Hartree-Fock energy to be the method which will be compared with our quantum simulations.

The energetic reference E_{ref} is, for each dimension of each distortion, the exact ground-state energy of the frozen-orbital system, which is obtained with a full numerical diagonalization of the eight-qubit Hamiltonian. Since it is the target energy, we refer to this energy as exact. This method is also very similar to a CASCI calculation; however, it takes into account CISD orbitals instead of Hartree-Fock orbitals. Each point of the simulations represents an average of 50 trials. In this work a trial consists of choosing an initial guess and using it with the VQE (with or without a model of noise).

In Fig. 4 we can see that the $v3$ circuit yields a lower energy compared to $v1$ and $v2$. The Hartree-Fock method, on the other hand, works better around the equilibrium position, but when the distortion start to be extreme, the system is in a position far from equilibrium and this hardware efficient circuit has a supreme performance in calculating the ground-state energy. The solution obtained with the $v1$ *Ansatz* is improved with depth, while the $v2$ and $v3$ *Ansätze* have their depth already optimal at $d = 1$. As the number of parameters in $v1$ and $v2$ is dN_{qubits} , we can conclude that there is no obvious link between the number of parameters and the accuracy.

For distortion 2, the $v3$ *Ansatz* is still supreme to its HE counterparts but it cannot manage to be closer than the Hartree-Fock energy. This difference from distortion 1 comes from the distortion itself: As Fig. 2 shows, in the case of distortion 1, when the distortion parameter is changed, all

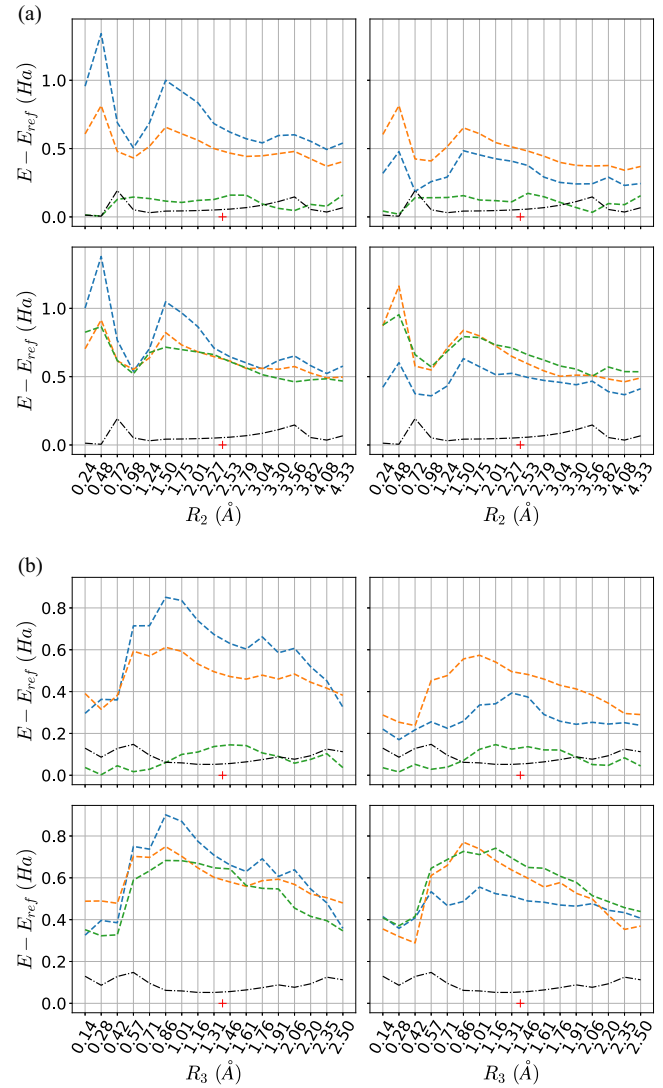


FIG. 5. Difference between the ground-state energy curves of the eight-qubit system obtained with the HE *Ansatz* for (a) the second distortion and (b) the third distortion, and the reference obtained with full diagonalization of the eight-qubit system.

the carbon atoms move. In the case of distortion 2, when the distortion parameter is changed, there are two pairs of carbon atoms that always have the same spacing, so their correlation is the same as the equilibrium position correlation. This can also explain why the Hartree-Fock method provides a better approximation in the case of distortion 2 than for distortion 1; its deviation from the target value is always lower than 0.2 Ha, while it reaches 0.4 Ha in distortion 1.

For the three distortions we can make the same general conclusions: The $v3$ circuit is supreme to $v1$ and $v2$ and the depth of the circuit impacts those results in a minor fashion. Around the equilibrium positions, the Hartree-Fock energy is more precise than these quantum methods; however, as we start to distort the system, the HE method gives better results. Eventually, these methods are rather complementary. Due to such a supreme performance of the $v3$ *Ansatz*, we will use only this HE *Ansatz* in the remaining sections of the paper. The supreme performance of the $v3$ *Ansatz* is somewhat

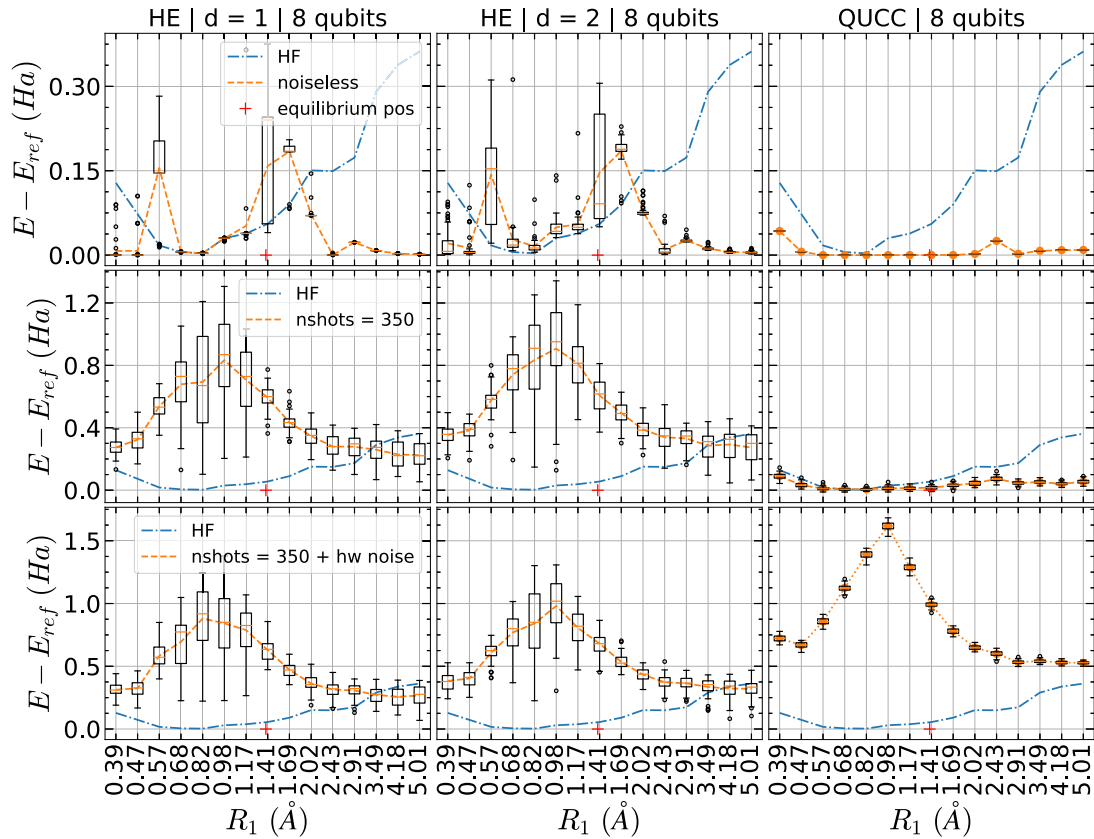


FIG. 6. Difference between the ground-state energies of the eight-qubit system obtained with the HE and QUCC *Ansätze* and the reference obtained with full diagonalization of the eight-qubit system. The box plots give an overview of the amplitude of the variations due to optimization, shot noise, and hardware noise issues. Each row shares the same y axis.

expected: It provides entanglement between neighboring qubits and has a large pool of single-qubit gates.

B. HE vs QUCC *Ansätze*

In this section we perform calculations in order to compare the HE method with different depths with the QUCC method, in the case of eight-qubit systems for each distortion. The reference E_{ref} is, for each length of each distortion case, the ground-state energy of the eight-qubit system, obtained by a full diagonalization of the active-space Hamiltonians of eight qubits. The optimizer is COBYLA with a maximum of 1000 iterations.

In Fig. 6 (see Fig. 7 for second and third distortions), the left and middle columns represent the ground-state energies obtained with the HE *Ansatz* with depths equal to 1 and 2, respectively. The right column shows the QUCC results. The top row displays noiseless simulations, while the middle and bottom rows show simulations with noise. The middle row corresponds to the simulations with shot noise only and the bottom row refers to simulations with both shot noise and hardware noise. Finally, the HE results of the top and bottom rows are the same as the results of Fig. 4. All the HE curves and the noisy QUCC curves displayed are the average of 50 trials, while the noiseless QUCC simulations are computed only one time.

The first thing that we direct attention to is the presence of box plots, which represents a variance in the multiple trials.

The box denotes where 50% of the values converge to, while the full 100% is between the whiskers. The single points represents results that are beyond 1.5 times the whisker size. This variance through the results is due to the choice of the initial guess and the optimizer itself. For the initial guess of parameters in the HE method we choose a random vector. As every new trial requires a new initial guess, the starting trial state is never the same, so at the end, the algorithm can be confined in a local minimum which depends heavily on the initial guess. This illustrates the shortcomings of the COBYLA optimizer, which is not robust enough to escape local minima and converge towards the global solution.

Generally, the noiseless simulation shows that the variance is higher around the equilibrium position. Moreover, the implementation of shot noise seems to equilibrate the variance across the results, and the consideration of hardware noise decreases the variance of the results, although this makes the HE method outperformed by classical methods.

Otherwise, the QUCC method has a very low variance, which can be explained by its accurate initial guess which seems to prevent the optimizer from converging towards a local minimum. In contrast to the HE method, the presence of hardware noise causes QUCC methods to give less good results compared to the HE method, a feature which is not too surprising given the large number of gates in the *Ansatz*. It is also important to point out that the QUCC method is much more sensitive to the hardware noise than to the shot noise.

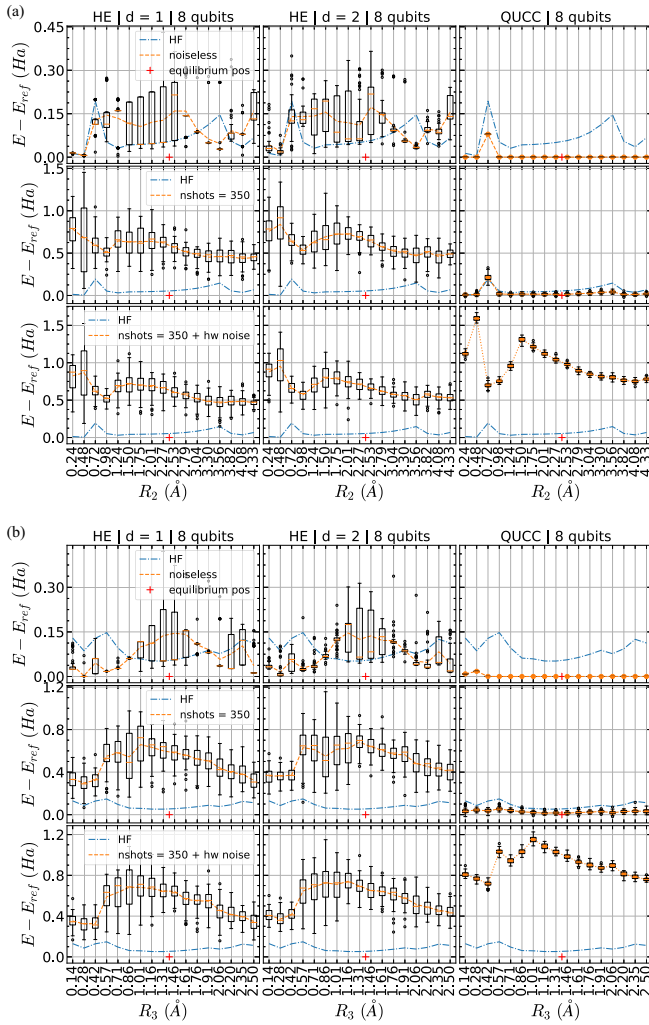


FIG. 7. Difference between the ground-state energies of the eight-qubit system obtained with the HE and QUCC *Ansätze* for (a) the second distortion and (b) the third distortion, and the reference obtained with full diagonalization of the eight-qubit system.

C. Optimization in QUCC simulations

In this section we focus on the QUCC simulations. We compare the initial guess of the QUCC method with its value obtained after optimization in Fig. 8 [see Figs. 9(a) and 9(b) for the second and third distortions]. The reference E_{ref} is, for each length of each distortion case, the ground-state energy of the N_{qubits} -qubit system (written on top of the columns), obtained with a full diagonalization of the active-space Hamiltonians of N_{qubits} qubits. The optimizer is COBYLA with a maximum of 1000 iterations. Each of the four columns of graphs corresponds to a different selection of the active orbital space in the system. Each row of graphs corresponds to a particular noise model. The top row displays noiseless simulations, while the two others show simulations with only shot noise, fixed at 1024 for the middle row and 350 for the bottom row. The initial guesses are single simulations. For the 4-, 8-, and 12-qubit systems, the noisy optimal guess with 350 shots displayed is an average of 50 trials. Except for these, all the optimal guesses are obtained with only one trial.

For each distortion, the eight-qubit case shows that the initial guess of the QUCC method is a really accurate guess. In particular, for certain lengths in the first distortion, the difference between the initial guess, the optimal guess, and the target energy is not perceptible at this scale. On the other hand, going from 4 to 12 qubits, the noiseless row illustrates that the difference between the initial guess and the optimal guess increases. However, when the number of qubits is 16 there is no substantial increase in precision between the initial guess and the optimal solution. This has to do with the fact that aromatic molecules such as benzene are well described with an active space of six orbitals (12 qubits). Indeed, the larger the system, the more parameters added. The more parameters one adds, the more iterations one needs to converge. This lack of iterations explains also why the 16-qubit optimal guesses seem to be higher in energy than the 12-qubit ones.

Concerning the noisy simulations, the important information is that the optimal energy may be higher than the initial guess, which we find quite surprising. We understand that this phenomenon is caused by quantum noise. Indeed, let us imagine an optimization surface: Increasing the level of noise decreases the smoothness of the optimization surface [29] and the harder it is to reach the real minimum energy. Moreover, the optimization surface dynamically changes between realizations; when the optimizer changes the parameters to check if there is a better solution, the presence of noise can prevent the optimizer from recovering the previous “better” solution.

D. Increasing the number of qubits

In this section we compare the results computed for the 4-, 8-, 12-, and 16-qubit systems, for the first distortion in Fig. 10. The top rows display the noiseless simulations, while the bottom rows show the simulations with shot and hardware noise, up to eight qubits due to capabilities of the QLM. Each column refers to a particular size of the system. The reference E_{ref} is, for each length of each distortion case, the ground-state energy of the 16-qubit system, obtained with a full diagonalization of the active-space Hamiltonians of 16 qubits. The optimizer is COBYLA with a maximum of 1000 iterations. The QUCC noiseless simulations are obtained with one trial, while the noisy ones are an average of 50 trials. All the HE calculations are the results of 50 trials, except for 16-qubit systems where there is only one trial due to the large computational times required to obtain more than one trial.

Generally, for each distortion in the noiseless row, the QUCC method is very accurate in the case of noiseless simulations and it outperforms the classical methods. Figures 10, 11(a), and 11(b) show that from eight-qubit systems to 12-qubit systems, the QUCC *Ansatz* provides decreasing energies, indicative of a better solution as a larger number of orbitals are activated.

The HE method has variable precision depending on the distortion and the size of the system. As said before, the applicability of the HE *Ansatz* is proportional to the level of distortion. Figure 10 shows explicitly that for extreme distortions, the HE method provides a better energy than the QUCC method and does so with the same maximum number of iterations.



FIG. 8. Comparison between initial and optimal guesses yielded by the QUCC Ansatz, for the first distortion, with E_{ref} being obtained with full diagonalization of the active-space Hamiltonian. The corresponding number of qubits is written on top of each column. All the figures share the same y axis. The noise increases from the top line to the bottom.

Likewise, when the deformation is less pronounced, the QUCC method and even the classical methods outperform the HE method, which gives an increasing energy as the system grows. This phenomenon, which occurs also in the second and the third distortion, can also be due to the maximum number of iterations available. Indeed, for both HE and QUCC methods, the number of parameters increases with the number of qubits; therefore, the convergence becomes more difficult with a growing system, while we have set our optimizer to maximally 1000 iterations throughout the paper. As in Sec. III C, this explains why the QUCC method seems to stagnate between an active orbital selection of 12 and 16 qubits.

Concerning the noisy simulations, the three distortions have mostly the same behavior. The QUCC method totally fails when one tries to include hardware noise, and even if the HE efficient method gives better results they are still suboptimal because both are outperformed by classical methods. One can also notice that the quantum methods are further from the reference around the equilibrium position than for extreme distortions, for which quantum methods provide a better solution.

E. Comparison of quantum and classical methodologies

In Fig. 12 we compare quantum computing methodologies with state-of-the-art classical computing methods for the first

distortion (similar results for distortions 2 and 3 can be found in Fig. 13). The natural orbital occupation numbers (NOONs) are estimated from classical solvers in Figs. 12(a)–12(c), the 12-qubit QUCC solution in Fig. 12(e), and the 16-qubit QUCC solution in Fig. 12(f). Figure 12(d) shows the NOONs obtained with the CASCI [48] calculation made on an active space of eight electrons in eight orbitals. Figure 12(g) displays the ground-state energy curve, in which the HE and QUCC results are the 16-qubit optimal guesses shown in Fig. 10. The black curve labeled “FDASH” corresponds to the ground-state energy of the 16-qubit systems obtained with a full diagonalization of the 16-qubit active-space Hamiltonians. The other energies are obtained with classical methods applied to the whole benzene system without orbital freezing.

In terms of energy [Fig. 12(e)], the MP2, CCSD, and CCSD(T) methods yield unphysical dissociation curves. The MP2 method starts to fail around $R_1 = 3.5$ Å and the CCSD and CCSD(T) methods start to fail around approximately $R_1 = 2.5$ Å. The CIPSI method has difficulty converging starting from $R_1 = 3.5$ Å. The CISD method gives a relatively low energy and a physical dissociation curve without local minima. From $R_1 = 2.5$ Å, there is a competition between dynamic and static correlations that is not captured by all methods, especially by the CCSD method, which is limited by its single-determinant nature. As said before, the QUCC method is very precise, especially around the equilibrium

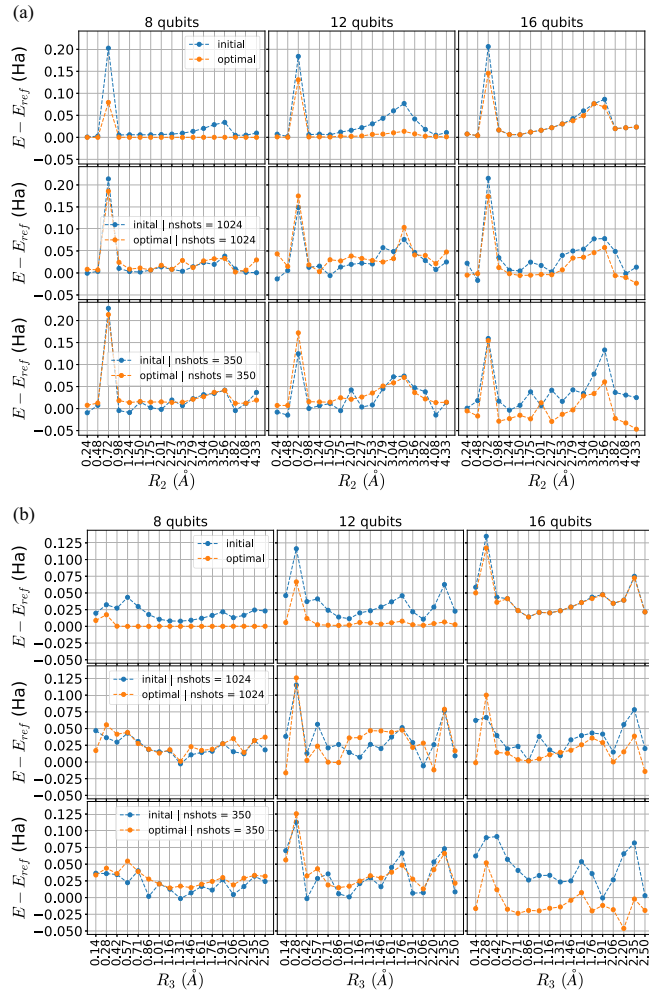


FIG. 9. Comparison between the initial and optimal guesses with the QUCC Ansatz for (a) the second distortion and (b) the third distortion, with E_{ref} the energies obtained with full diagonalization of the active-space Hamiltonian. The corresponding number of qubits is written on top of each column.

position, while the HE method gives results very close to the reference energy when the system is strongly distorted. The MP2 and CCSD energetic behavior can be understood with the NOONs [Fig. 12(d)]. Indeed, when distortion 1 is applied to benzene, we are artificially creating six C—H pairs. Due to the symmetry of the chemical system, we expect, for extreme distortions, to avoid the interaction between these pairs and then to have noninteracting orbitals with the same energy, which results in orbitals with the same occupation number. However, MP2 and CCSD NOONs fail for the same geometries in which the energies are nonphysical, while the CISD method gives more realistic NOONs. Here the CASCI NOONs act as a reference for the QUCC NOONs. Not only do the QUCC NOONs show explicitly the expected phenomena: The occupation numbers of natural orbitals (NOs) 2–7 are gathering as R_1 is increasing, but also one can notice that the QUCC 12-qubit NOONs match the CASCI NOONs much better than the QUCC 16-qubit results. This explains the convergence issues detailed in Sec. III E between the 12-

and 16-qubit results: By taking NOs 1 and 8 into consideration, the optimization cost increases unnecessarily with parametrizing orbitals that are already well described when frozen. This phenomenon, coupled with a limited number of optimizations steps, yields difficulties for solving larger systems on real quantum computers, even without taking into consideration the noise: At $R_1 = 1.41$ Å, $E(\text{CIPSI}_{\text{full}}) - E(\text{QUCC}_{16 \text{ qubits}}) = 0.33$ Ha, which means that even if active-space selection induces errors that theoretically disappear when increasing the size of the system, in practice optimization problems start inducing significant errors. In addition, it confirms the validity of the Hückel approximation as NO 1 and NO 8 remain frozen whatever the distortion.

F. Robustness against noise

In this section we compare the robustness against the shot and decoherence noise of the HE and QUCC Ansatz at the equilibrium point. Following some interesting works about the noise effects on VQE calculations [49–52], we aim to go into more detail about some noise effects when treating such a complex system as benzene. Taking gate durations indicated in Table I and setting $T_2 = T_1$, we calculated the ground-state energy of the eight-qubit active-space Hamiltonian benzene, for $R_1 = 1.41$ Å, with T_1 varying from 80 to 1000 μs . Figure 14 shows the average of ten trials obtained with the QUCC Ansatz and the average of 50 trials obtained with the HE Ansatz. Here “HE” refers to the calculations made with a random initial guess, while “HE_0” always had the same initial guess, which was zero. Each trial is computed with 1024 shots for the top row and 4096 shots for the bottom one. The dashed curves with square markers are the average of trials, while the shaded area represents the amplitude of variation through the trials. While the whole VQE algorithm was used for the simulations, only the last optimization step (obtained in a noiseless case) was taken and we launched it on an actual quantum computer IBMQ_Toronto, which has T_1 and T_2 approximately at 100 μs . This was done in order to estimate the effect of noise on the estimation for the expectation value itself as estimating the noise during the classical optimization process would run beyond the scope of this paper. The stars denotes the average of ten demonstrations, and maximum and minimum values are represented by horizontal lines.

This figure shows that increasing the number of shots does not have obvious consequences and it confirms some claims made in Sec. III B. First, one can see that from 1024 to 4096 shots the variance of the QUCC results decreases while the average remains constant. This confirms that the QUCC method is much more affected by decoherence noise than by measurement noise. Furthermore, for the HE results it is the opposite: The average has dropped by 0.2 Ha, independently of T_1 , while the variance of HE results has the same order of magnitude. This confirms the greater sensibility of the HE Ansatz to shot noise than to hardware noise. On the other hand, for HE_0 results, neither the average nor the variance changed when increasing the number of shots. This seems to illustrate that some areas of the optimization landscape are robust against noise; initializing a state in $|0\rangle \otimes \dots \oplus |0\rangle$ makes it more immune against qubit relaxation than any string

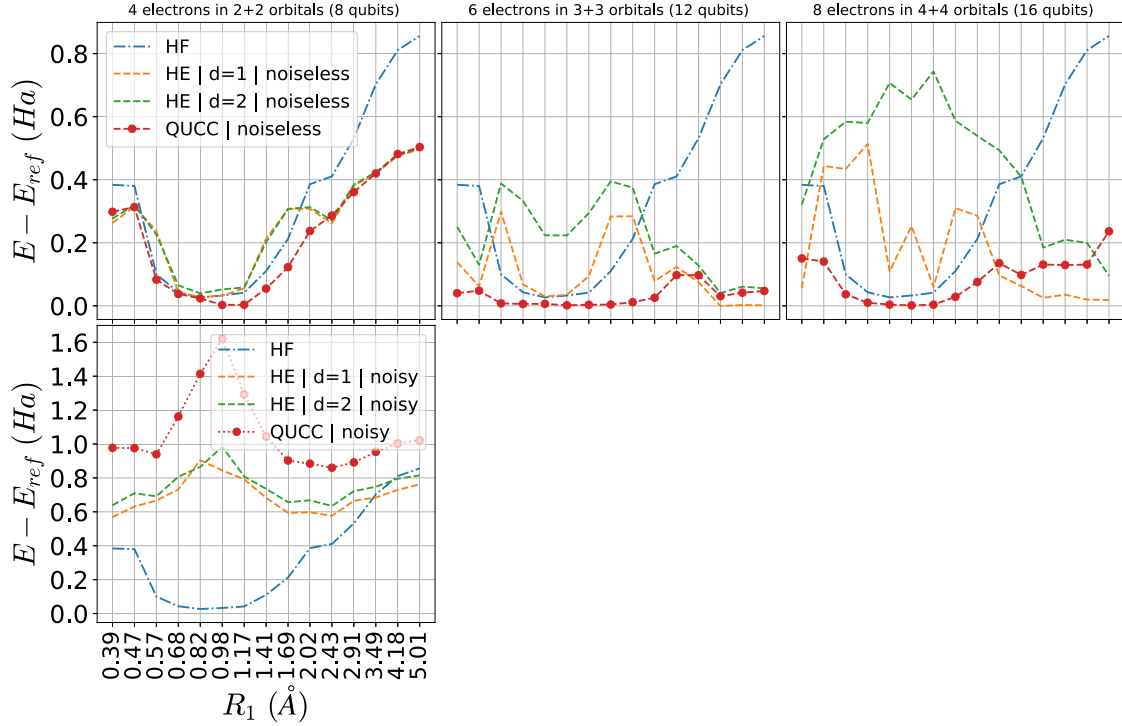


FIG. 10. Comparison of the ground-state energy curves of different numbers of qubits obtained with different methods, for the first distortion. Here E_{ref} is the energy obtained with full diagonalization of the 16-qubit active-space Hamiltonian. Each row share the same y axis.

involving $|1\rangle$ would be. In addition, the difference between extreme values is 0.34 Ha for the HE *Ansatz* without noise (Fig. 5, top row and left column), 0.46 Ha for the HE *Ansatz* with noise, and 0.15 Ha for HE₀ with noise. This shows that, for the HE *Ansatz*, the choice of a random initial guess has a higher impact on the convergence than the noise itself. On the other hand, an extrapolation of QUCC results yields $T_1 \geq 36$ ms to reach a 10^{-2} precision, or $T_1 \geq 3.6$ s to be close to within 10^{-4} of the reference. This gives numerical confirmation that the QUCC *Ansatz* will never be compatible with actual noisy intermediate-scale quantum (NISQ) hardware without noise mitigation.

Regarding real QPU calculations, even if the QUCC results are quite close to the noise model both quantitatively and qualitatively, the HE results are a bit further away from it despite the slight overlap between the HE error bar and shaded area. However, our noise model is simplified and the values for T_1 and T_2 change dynamically between calibrations of the IBM Quantum hardware. Furthermore, the connectivity of the IBM Quantum hardware is not all to all and this is compensated with additional SWAP gates.

In Fig. 15 we compare the results obtained with our noise model (see Table I) with real QPU calculations due to IBMQ_Toronto, for eight-qubit active-space Hamiltonians of benzene under distortion 1. As before, the VQE has been fully used in our noise model case, and only the last optimization step (yield by a noiseless computation loop) was processed on quantum computer. The dashed curve corresponds to the noise model and holds an average of 50 trials, while the shaded area illustrates the amplitude of variation of the results. The stars

correspond to an average of ten real QPU demonstrations, with maximum and minimum values represented by horizontal dashes. In both case, the reference is the ground-state energy of the eight-qubit system, obtained by a full diagonalization of the active-space Hamiltonians of eight qubits.

First, one can see that the average of the QUCC demonstrations matches quite well our noise model, while the average of the HE demonstrations is less than 0.3 Ha away from it. However, despite the slight quantitative gap between the HE *Ansatz* results on QPUs and HPCs, the error bars are close to the value obtained for the noise model. One can also notice that the curves have the same shape, meaning that the influence of noise with R_1 is similar in both situations. In particular, the noise dominates much more around the equilibrium position than for extreme distortions, which confirms the previous statements. This can also be seen in the 16-qubit results (see Fig. 16). Moreover, increasing the number of shots has no significant impact on the average of demonstrations but it decreases the variance of the results. From a more chemical point of view, even for extreme distortions, actual QPUs with the HE *Ansatz* would not enable one to outperform the HF calculations.

IV. CONCLUSION

We have estimated the feasibility to execute families of hardware efficient quantum computing *Ansätze* and quantum unitary coupled-cluster *Ansätze* on near-term quantum computers. By incorporating a realistic noise model, we found that hardware efficient *Ansätze* could be executed on near-term

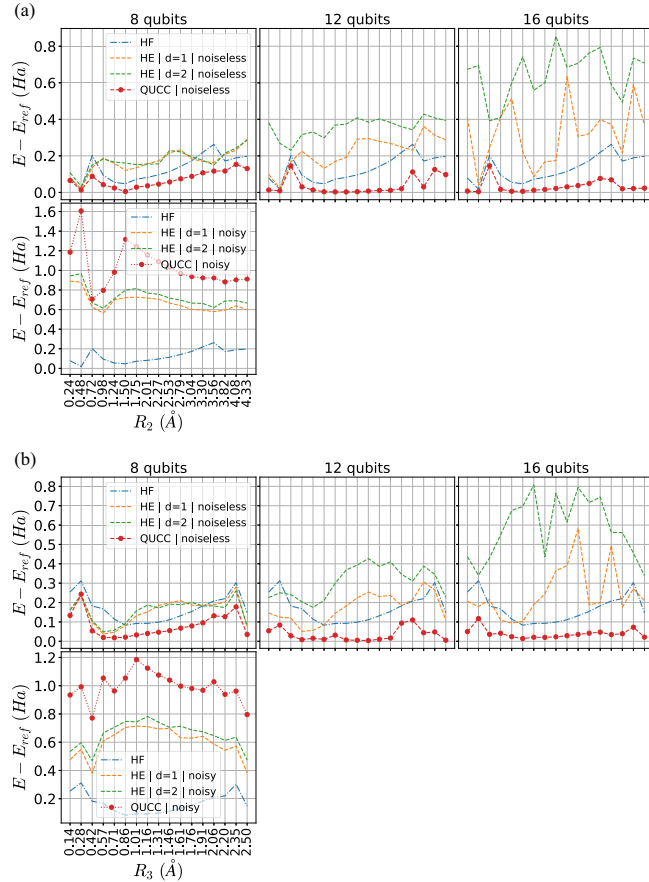


FIG. 11. Comparison of ground-state energy curves of different numbers of qubits, for (a) the second distortion and (b) the third distortion, with the reference energy being obtained with full diagonalization of the active-space Hamiltonian. The corresponding number of qubits is written on top of each panel in the top row of (a) and (b).

hardware, giving better precision than mean-field methods far away from the charge equilibrium point. In contrast, the QUCC method is superior to mean-field methods but will remain a method for simulators in the pre-error-correction era. The QUCC method also preserves well the particle number of individual orbitals. Noise remains a central issue, particularly around the equilibrium position. For all approaches, noise appears as a consequence, but its importance is shown to be more critical in the case of the QUCC *Ansatz*, which could be a nonoperational method on the NISQ era real quantum computers for such a large system as benzene. Real demonstrations on the IBM Quantum show that our noise model describes well the noisy operation of a QPU both qualitatively and somewhat quantitatively. Overall, more research is needed to develop advanced noise-resistant *Ansätze*, especially for those based on the QUCC method. Regarding the fact that the QUCC method is much more sensitive to the hardware noise than to the shot noise and knowing that reaching an unlimited number of measurements seems difficult on a real machine, it seems important to work out noise-reduction techniques in this particular area. In addition, *Ansätze* continue to evolve

and recent works directed toward VQEs may improve the robustness of QUCC-based methodologies in the near future [53,54]. Anecdotally, although adapt-VQE methodologies are state of the art on the algorithmic side for QPUs, the number of gradients to be calculated remains a huge problem for practical implementation [22]. Indeed, the large number of gradient evaluations scales suboptimally with system size and would overconsume actual QPU resources. Making a calculation on a real QPU requires a compromise between circuit depth and number of executions. Thus we foresee that if adapt-VQE-like algorithms would reduce circuit depth, they will also enhance the complexity of each execution. In this form, it would have a limited impact on large systems, especially in the NISQ era, as system size is limited not only by the noise but also by the optimizations issues that strongly increase with it. Therefore, our future path should be directed towards solving this problem.

Our findings further suggest that the HE *Ansatz* is sensitive to the random initial guess of the parameters, commonly leading to false minima of the optimizer. Furthermore, increasing the size of the active space can lead to a similar result, a solution which is trapped in a local minimum. Finally, in contrast to classical methods, quantum computing methodologies manage to preserve physically relevant orbital occupancies.

ACKNOWLEDGMENTS

We acknowledge Mohammad Haidar for the classical simulations and Jan Reiner and Arseny Kovyshin for useful discussions. W.S. and M.J.R. acknowledge funding from European Union's Horizon 2020 Research and Innovation Program, more specifically, the (NE|AS|QC) project under Grant Agreement No. 951821. This work has also received funding from the European Research Council (ERC) under the European Union's Horizon 2020 Research and Innovation Program (Grant Agreement No. 810367), project EMC2 (J.-P.P.).

APPENDIX A: SECOND QUANTIZATION HAMILTONIAN

Generally, a molecule is composed of atoms, which are composed of nuclei and electrons. The Hamiltonian of any molecule can be written as

$$H = T + V, \quad (\text{A1})$$

with T the kinetic energy operator and V the potential energy operator. Using atomic units, T describes the movement of the particles and V describes the Coulomb interaction between them:

$$T = -\underbrace{\sum_{i=1}^N \frac{1}{2} \nabla_i^2}_{\text{electron}} - \underbrace{\sum_{A=1}^M \frac{1}{2} \nabla_A^2}_{\text{nuclei}}, \quad (\text{A2})$$

$$V = -\underbrace{\sum_{i,A} \frac{Z_A}{r_{iA}}}_{\text{electron-nuclei}} + \underbrace{\sum_{j>i} \frac{1}{r_{ij}}}_{\text{electron-electron}} + \underbrace{\sum_{B>A} \frac{Z_A Z_B}{r_{AB}}}_{\text{nuclei-nuclei}}. \quad (\text{A3})$$

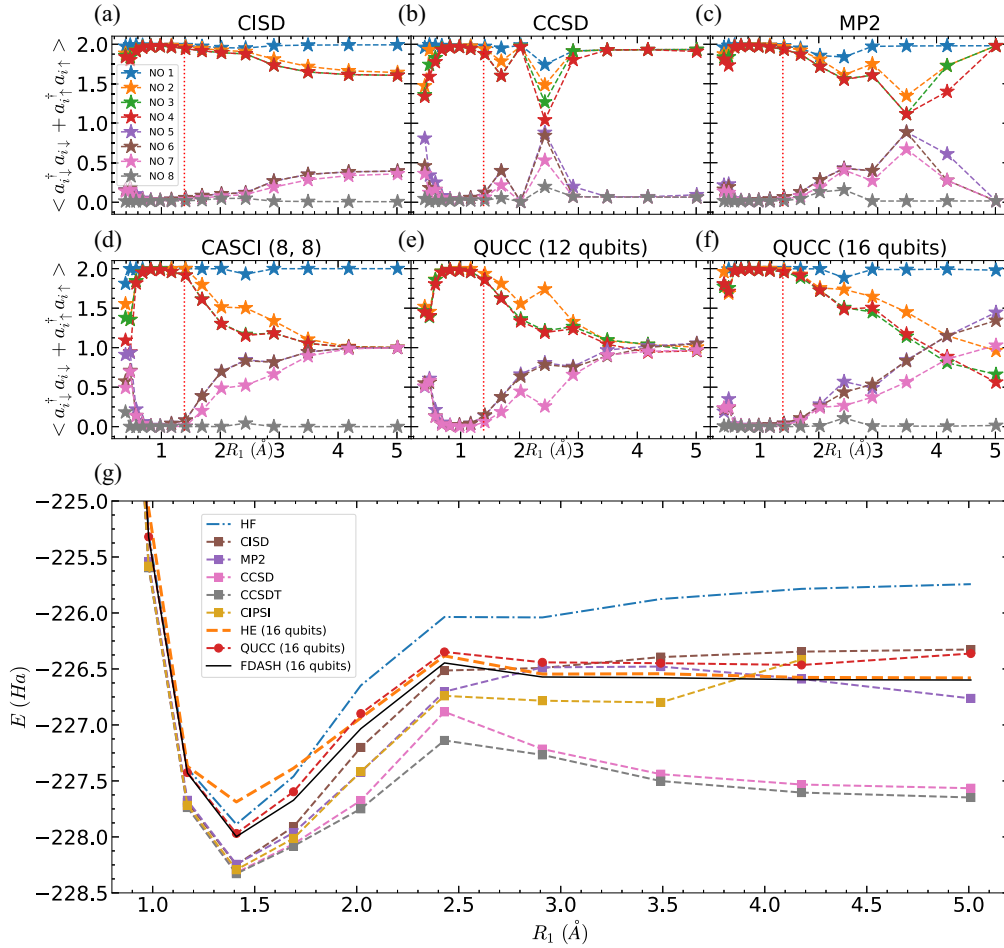


FIG. 12. NOONs obtained with the (a) CISD, (b) CCSD, (c) MP2, (d) CASCI, and (e) and (f) QUCC methods for distortion 1 (a)–(c) through a calculation on the whole benzene system and (d)–(f) within different active-space selections. They all share the same axis. The vertical red dashed line indicates the equilibrium geometry. (g) Ground-state energy curves obtained with different methodologies. Here and in the following figures FDASH stands for full diagonalization of the active-space Hamiltonian.

These equations are simplified when one works with the Born-Oppenheimer approximations, by neglecting the kinetic energy term of nuclei and the Coulomb interaction term between them. So the Hamiltonian is

$$H = -\sum_i \frac{1}{2} \nabla_i^2 - \sum_{i,A} \frac{Z_A}{r_{iA}} + \sum_{j>i} \frac{1}{r_{ij}}. \quad (\text{A4})$$

The principle of second quantization consists in rewriting the Hamiltonian with the creation and annihilation operators a^\dagger and a , respectively, which acts on the occupation number vector

$$H = \sum_{p,q} h_{pq} a_p^\dagger a_q + \sum_{p,q,r,s} \frac{h_{pqrs}}{2} a_p^\dagger a_q^\dagger a_r a_s. \quad (\text{A5})$$

The first term describes both the kinetic energy and the Coulomb interaction with nuclei of an electron, while the second term describes the two-body Coulomb interaction be-

tween pairs of electrons. With $\mathbf{x} = (\mathbf{r}, \sigma)$, these terms can be written as

$$h_{pq} = \int d\mathbf{x} \phi_p^*(\mathbf{x}) \left(-\frac{1}{2} \nabla^2 - \sum_A \frac{Z_A}{|\mathbf{r} - R_A|} \right) \phi_q(\mathbf{x}) \forall p, q, \quad (\text{A6})$$

$$h_{pqrs} = \int d\mathbf{x}_1 d\mathbf{x}_2 \phi_p^*(\mathbf{x}_1) \phi_q^*(\mathbf{x}_2) \times \left(\frac{1}{|\mathbf{r}_1 - \mathbf{r}_2|} \right) \phi_r(\mathbf{x}_1) \phi_s(\mathbf{x}_2) \forall p, q, r, s. \quad (\text{A7})$$

Each $\phi(\mathbf{x}) = \phi(\mathbf{r}, s)$ represents a spin orbital of the basis set. Finally, the more elaborate the basis set, the larger the Hamiltonian: If we stick with a basis with N_{orb} orbitals, then it has $2N_{\text{orb}}$ spin orbitals, which results in a full Hamiltonian stored in a $(2^{2N_{\text{orb}}}, 2^{2N_{\text{orb}}})$ matrix.

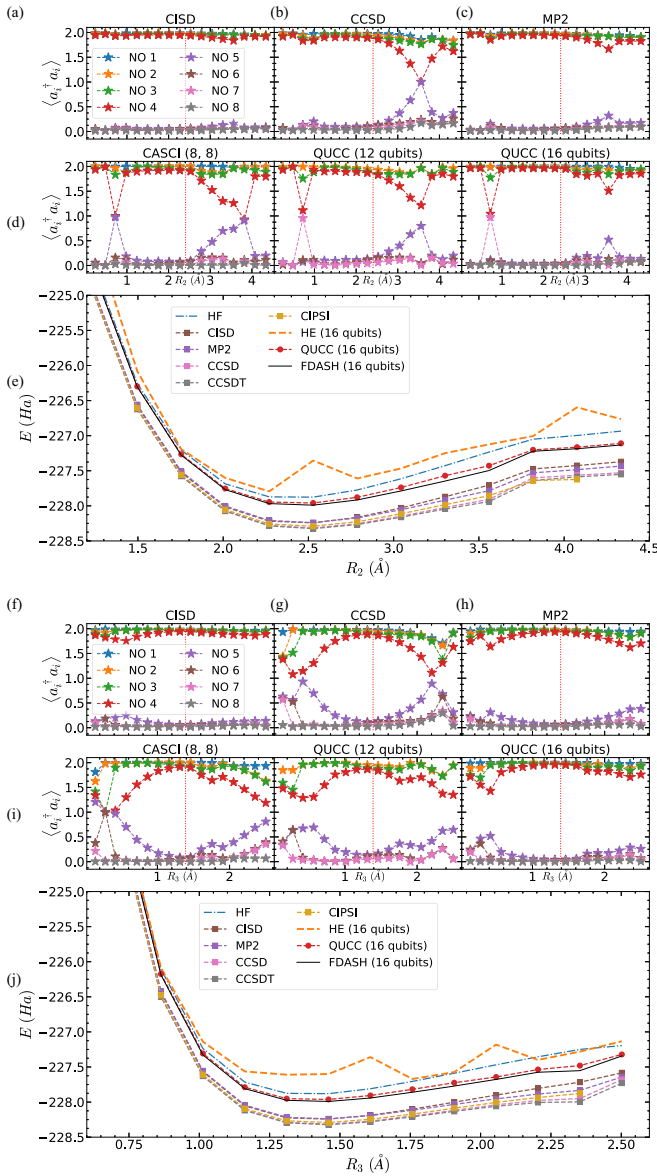


FIG. 13. NOONs obtained with the (a) and (h) CISD, (b) and (i) CCSD, (c) and (j) MP2, (d) and (k) CASCI, and (e) and (l), and (f) and (m) QUCC methods for distortions 2 and 3, respectively. (a)–(c) and (h)–(j) were obtained through a calculation on the whole benzene system while (d)–(f) and (k)–(m) were obtained within different active-space selections. They all share the same axis. The vertical red dashed line indicates the equilibrium geometry. (g) and (n) Ground-state energy curves obtained with different methodologies.

APPENDIX B: JORDAN-WIGNER TRANSFORMATION

Quantum computers are composed of qubits, whose state is modified by rotations in the Bloch sphere, which are performed by single-qubit quantum gates. In order to be understandable by quantum computers, the second quantized Hamiltonian has to be transformed into a new form, obeying the fermionic algebra of electrons but also behaving similarly to the $SU(2)$ group behavior of qubits. While the occupation number vector is quite easy to transform, by asserting a qubit

to $|0\rangle$ if a spin orbital is empty and $|1\rangle$ if a spin orbital contains an electron, the main problem is the conservation of the antisymmetric properties of the system. The Jordan-Wigner transformation converts the creation and annihilation operators while preserving their antisymmetric properties [55]:

$$a_i^\dagger \rightarrow \left(\prod_{j<i} \sigma_j^Z \right) \frac{\sigma_i^X - i\sigma_i^Y}{2} \quad \forall i < N_{\text{qubits}}, \quad (\text{B1})$$

$$a_i \rightarrow \left(\prod_{j<i} \sigma_j^Z \right) \frac{\sigma_i^X + i\sigma_i^Y}{2} \quad \forall i < N_{\text{qubits}}. \quad (\text{B2})$$

Finally, the Hamiltonian of the system can be written as a sum of Pauli strings [30]

$$H_{\text{JW}} = \sum_j h_j P_j. \quad (\text{B3})$$

APPENDIX C: IDLE NOISE MODEL

Briefly, let us consider a qubit in the state $|\phi\rangle = \alpha|0\rangle + \beta|1\rangle$. The density matrix ρ_0 of the pure state is

$$\rho_0 = |\phi\rangle\langle\phi| = \begin{pmatrix} |\alpha|^2 & \alpha\beta^* \\ \alpha^*\beta & |\beta|^2 \end{pmatrix}. \quad (\text{C1})$$

The Kraus operators for pure dephasing [56,57] are, with $p_{\text{ph}}(t)$ the decaying law of the phase,

$$E_0 = \begin{pmatrix} 1 & 0 \\ 0 & \sqrt{1-p_{\text{ph}}(t)} \end{pmatrix}, \quad E_1 = \begin{pmatrix} 0 & 0 \\ 0 & \sqrt{p_{\text{ph}}(t)} \end{pmatrix}. \quad (\text{C2})$$

Then the density matrix which takes into account this phenomenon becomes

$$\rho = \sum_k E_k \rho_0 E_k^\dagger = \begin{pmatrix} |\alpha|^2 & \alpha\beta^* \sqrt{1-p_{\text{ph}}(t)} \\ \alpha^*\beta \sqrt{1-p_{\text{ph}}(t)} & |\beta|^2 \end{pmatrix}. \quad (\text{C3})$$

Moreover, the Kraus operators for amplitude damping are, with $p_a(t)$ the decreasing law of the amplitude,

$$E_0 = \begin{pmatrix} 1 & 0 \\ 0 & \sqrt{1-p_a(t)} \end{pmatrix}, \quad E_1 = \begin{pmatrix} 0 & \sqrt{p_a(t)} \\ 0 & 0 \end{pmatrix}. \quad (\text{C4})$$

Then the density matrix which takes into account this phenomenon becomes

$$\rho = \begin{pmatrix} |\alpha|^2 + |\beta|^2 p_a(t) & \alpha\beta^* \sqrt{1-p_{\text{ph}}(t)} \\ \alpha^*\beta \sqrt{1-p_{\text{ph}}(t)} & |\beta|^2 [1-p_a(t)] \end{pmatrix}. \quad (\text{C5})$$

At the end, one remarks that the pure dephasing impacts only the off-diagonal terms. Therefore, we can rewrite the density matrix for the two combined phenomena, and considering

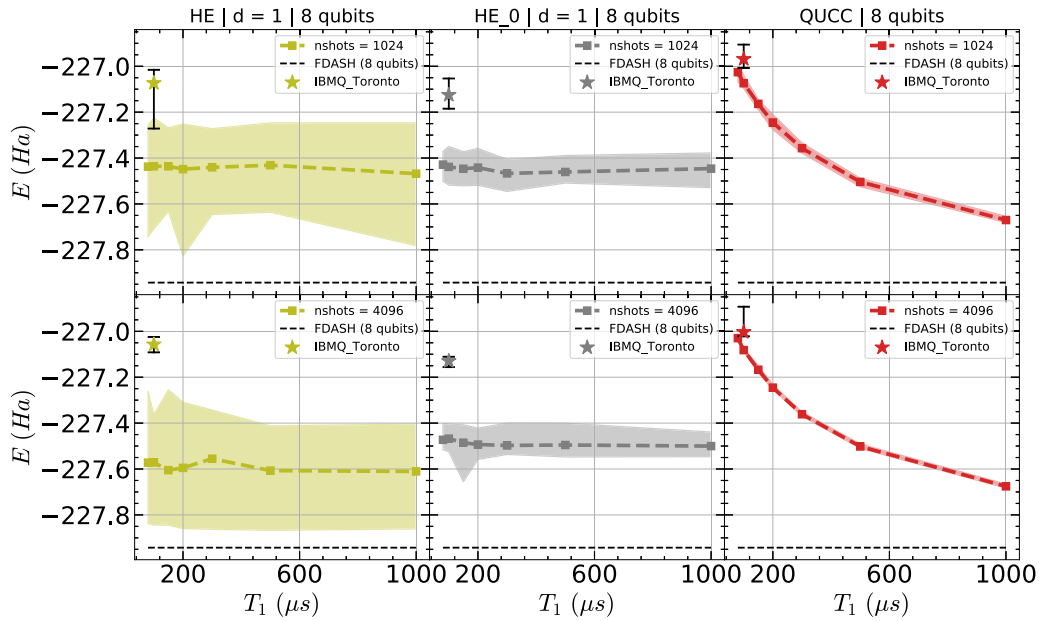


FIG. 14. Ground-state energy of the active-space Hamiltonian of eight qubits of benzene at $R_1 = 1.41 \text{ \AA}$, as a function of T_1 . The curves are noisy simulations while the stars were obtained with IBMQ_Toronto. The top row shows results with 1024 shots and the bottom one with 4096 shots. They share the same y axis.

time-exponential relaxations $p_a(t) = 1 - e^{-t/T_1}$ and $p_{ph}(t) = 1 - e^{-2t/T_2}$,

$$\rho = \begin{pmatrix} |\alpha|^2 + |\beta|^2(1 - e^{-t/T_1}) & \alpha\beta^*e^{-t/T_2'} \\ \alpha^*\beta e^{-t/T_2'} & |\beta|^2e^{-t/T_1} \end{pmatrix}, \quad (\text{C6})$$

with T_2' defined as $\frac{1}{T_2'} = \frac{1}{T_2} + \frac{1}{2T_1}$. Generalized to the whole qubit register, one is able to incorporate the effect of noise in the simulations.

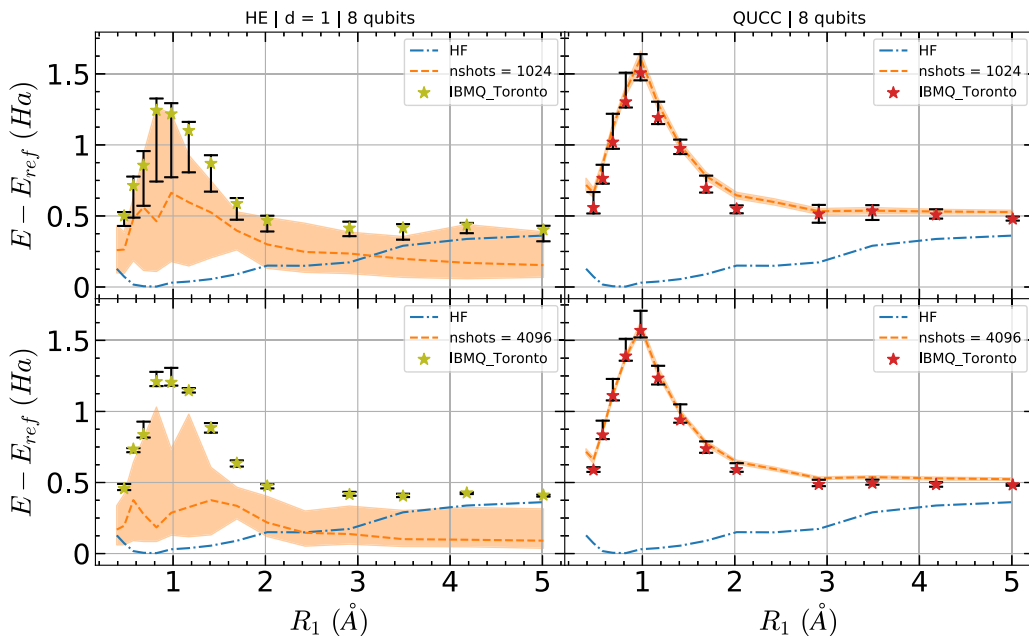


FIG. 15. Difference between the ground-state energies of the eight-qubit system obtained with the HE and QUCC *Ansätze*, with either our noise model or the real IBMQ_Toronto, and the reference obtained with full diagonalization of the eight-qubit system, for the first distortion. The top row shows results with 1024 shots and the bottom one with 4096 shots. All figures share the same y axis.

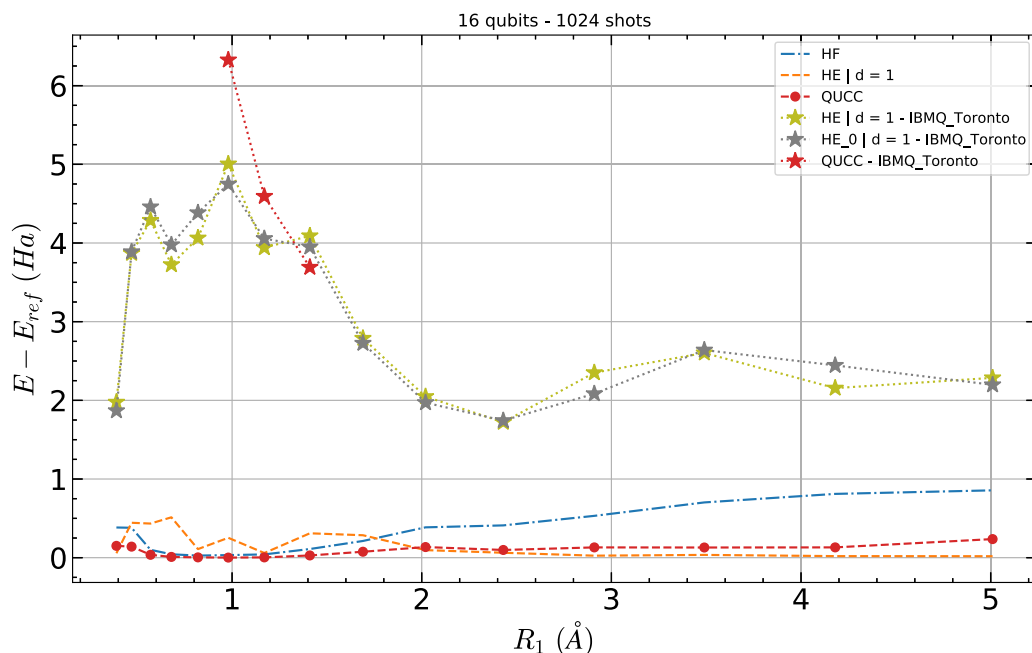


FIG. 16. Difference between the ground-state energies of the 16-qubit systems obtained with the HE and QUCC *Ansätze*, for the first distortion. Dashed lines are obtained with noiseless simulations using the QLM, while the real IBMQ_Toronto demonstrations are shown with stars. The reference is obtained with full diagonalization of 16-qubit active-space Hamiltonians. The effect of noise has the same behavior with R_1 as in the eight-qubit case (Fig. 15 in Sec. III D), although the order of magnitude is larger. Not all values are available due to interoperability issues.

- [1] L. K. Grover, in *Proceedings of the 28th Annual ACM Symposium on Theory of Computing, Philadelphia, 1996* (ACM, New York, 1996), pp. 212–219.
- [2] P. W. Shor, *SIAM Rev.* **41**, 303 (1999).
- [3] D. S. Abrams and S. Lloyd, *Phys. Rev. Lett.* **83**, 5162 (1999).
- [4] H. Mohammadbagherpoor, Y.-H. Oh, P. Dreher, A. Singh, X. Yu, and A. J. Rindos, in *Proceedings of the 2019 IEEE International Conference on Rebooting Computing (ICRC)* (IEEE, Piscataway, 2019), pp. 1–9.
- [5] A. Aspuru-Guzik, A. D. Dutoi, P. J. Love, and M. Head-Gordon, *Science* **309**, 1704 (2005).
- [6] D. A. Fedorov, B. Peng, N. Govind, and Y. Alexeev, *Mater. Theory* **6**, 1 (2022).
- [7] A. Peruzzo, J. McClean, P. Shadbolt, M.-H. Yung, X.-Q. Zhou, P. J. Love, A. Aspuru-Guzik, and J. L. O’Brien, *Nat. Commun.* **5**, 4213 (2014).
- [8] R. M. Parrish, E. G. Hohenstein, P. L. McMahon, and T. J. Martínez, *Phys. Rev. Lett.* **122**, 230401 (2019).
- [9] K. Bharti and T. Haug, *Phys. Rev. A* **104**, L050401 (2021).
- [10] J.-G. Liu, Y.-H. Zhang, Y. Wan, and L. Wang, *Phys. Rev. Res.* **1**, 023025 (2019).
- [11] K. M. Nakanishi, K. Mitarai, and K. Fujii, *Phys. Rev. Res.* **1**, 033062 (2019).
- [12] K. Fujii, K. Mizuta, H. Ueda, K. Mitarai, W. Mizukami, and Y. O. Nakagawa, *PRX Quantum* **3**, 010346 (2022).
- [13] A. Garcia-Saez and J. I. Latorre, [arXiv:1806.02287v1](https://arxiv.org/abs/1806.02287v1).
- [14] M. Cerezo, K. Sharma, A. Arrasmith, and P. J. Coles, *npj Quantum Inf.* **8**, 113 (2022).
- [15] D. Wang, O. Higgott, and S. Brierley, *Phys. Rev. Lett.* **122**, 140504 (2019).
- [16] K. Temme, S. Bravyi, and J. M. Gambetta, *Phys. Rev. Lett.* **119**, 180509 (2017).
- [17] Y. Li and S. C. Benjamin, *Phys. Rev. X* **7**, 021050 (2017).
- [18] E. Lewars, *Computational Chemistry* (Springer, Berlin, 2011).
- [19] Google AI Quantum and Collaborators, F. Arute, K. Arya, R. Babbush, D. Bacon, J. C. Bardin, R. Barends, S. Boixo, M. Broughton, B. B. Buckley *et al.*, *Science* **369**, 1084 (2020).
- [20] I. O. Sokolov, P. K. Barkoutsos, P. J. Ollitrault, D. Greenberg, J. Rice, M. Pistoia, and I. Tavernelli, *J. Chem. Phys.* **152**, 124107 (2020).
- [21] E. Rossi, G. L. Bendazzoli, S. Evangelisti, and D. Maynau, *Chem. Phys. Lett.* **310**, 530 (1999).
- [22] M. Haidar, M. J. Rančić, T. Ayril, Y. Maday, and J.-P. Piquemal, [arXiv:2206.08798v4](https://arxiv.org/abs/2206.08798v4).
- [23] W. Sennane and M. J. Rančić, Code for reproducing the study, available at <https://github.com/NEASQC/D4.2>.
- [24] Q. Sun, T. C. Berkelbach, N. S. Blunt, G. H. Booth, S. Guo, Z. Li, J. Liu, J. D. McClain, E. R. Sayfutyarova, S. Sharma *et al.*, *WIREs Comput. Mol. Sci.* **8**, e1340 (2018).
- [25] Q. Sun, X. Zhang, S. Banerjee, P. Bao, M. Barbry, N. S. Blunt, N. A. Bogdanov, G. H. Booth, J. Chen, Z.-H. Cui *et al.*, *J. Chem. Phys.* **153**, 024109 (2020).
- [26] P.-F. Loos, Y. Damour, and A. Scemama, *J. Chem. Phys.* **153**, 176101 (2020).
- [27] Y. Garniron, T. Applencourt, K. Gasperich, A. Benali, A. Ferté, J. Paquier, B. Pradines, R. Assaraf, P. Reinhardt, J. Toulouse *et al.*, *J. Chem. Theory Comput.* **15**, 3591 (2019).
- [28] E. Höckel, *Z. Phys.* **72**, 310 (1931).
- [29] W. Lavrijsen, A. Tudor, J. Müller, C. Iancu, and W. De Jong, in *Proceedings of the 2020 IEEE International Conference on Quantum Computing and Engineering (QCE)* (IEEE, Piscataway, 2020), pp. 267–277.

- [30] N. Moll, P. Barkoutsos, L. S. Bishop, J. M. Chow, A. Cross, D. J. Egger, S. Filipp, A. Fuhrer, J. M. Gambetta, M. Ganzhorn *et al.*, *Quantum Sci. Technol.* **3**, 030503 (2018).
- [31] W. Mizukami, K. Mitarai, Y. O. Nakagawa, T. Yamamoto, T. Yan, and Y.-y. Ohnishi, *Phys. Rev. Res.* **2**, 033421 (2020).
- [32] J. Lee, W. J. Huggins, M. Head-Gordon, and K. B. Whaley, *J. Chem. Theory Comput.* **15**, 311 (2019).
- [33] A. G. Taube and R. J. Bartlett, *Int. J. Quantum Chem.* **106**, 3393 (2006).
- [34] A. Kandala, A. Mezzacapo, K. Temme, M. Takita, M. Brink, J. M. Chow, and J. M. Gambetta, *Nature (London)* **549**, 242 (2017).
- [35] B. T. Gard, L. Zhu, G. S. Barron, N. J. Mayhall, S. E. Economou, and E. Barnes, *npj Quantum Inf.* **6**, 10 (2020).
- [36] H. L. Tang, V. O. Shkolnikov, G. S. Barron, H. R. Grimsley, N. J. Mayhall, E. Barnes, and S. E. Economou, *PRX Quantum* **2**, 020310 (2021).
- [37] A. G. Rattew, S. Hu, M. Pistoia, R. Chen, and S. Wood, [arXiv:1910.09694v4](https://arxiv.org/abs/1910.09694v4).
- [38] M. A. Nielsen and I. Chuang, *Quantum Computation and Quantum Information* (American Association of Physics Teachers, College Park, 2002).
- [39] N. Hatano and M. Suzuki, *Quantum Annealing and Other Optimization Methods* (Springer, Berlin, 2005), pp. 37–68.
- [40] M. Brune, E. Hagley, J. Dreyer, X. Maitre, A. Maali, C. Wunderlich, J. M. Raimond, and S. Haroche, *Phys. Rev. Lett.* **77**, 4887 (1996).
- [41] C. L. Degen, F. Reinhard, and P. Cappellaro, *Rev. Mod. Phys.* **89**, 035002 (2017).
- [42] V. Frey, L. M. Norris, L. Viola, and M. J. Biercuk, *Phys. Rev. Appl.* **14**, 024021 (2020).
- [43] S. Nakajima, *Prog. Theor. Phys.* **20**, 948 (1958).
- [44] R. Zwanzig, *J. Chem. Phys.* **33**, 1338 (1960).
- [45] P. Krantz, M. Kjaergaard, F. Yan, T. P. Orlando, S. Gustavsson, and W. D. Oliver, *Appl. Phys. Rev.* **6**, 021318 (2019).
- [46] S. Martina, L. Buffoni, S. Gherardini, and F. Caruso, *Quantum Machine Intelligence* **4**, 8 (2022).
- [47] H.-P. Breuer and F. Petruccione, *The Theory of Open Quantum Systems* (Oxford University Press on Demand, 2002).
- [48] T. Helgaker, P. Jorgensen, and J. Olsen, *Molecular Electronic-Structure Theory* (Wiley, New York, 2014).
- [49] E. Fontana, N. Fitzpatrick, D. M. Ramo, R. Duncan, and I. Rungger, *Phys. Rev. A* **104**, 022403 (2021).
- [50] C. Ding, X.-Y. Xu, S. Zhang, W.-S. Bao, and H.-L. Huang, [arXiv:2208.05378](https://arxiv.org/abs/2208.05378).
- [51] W. Saib, P. Wallden, and I. Akhalwaya, in *Proceedings of the 2021 IEEE International Conference on Quantum Computing and Engineering (QCE)* (IEEE, Piscataway, 2021), pp. 42–53.
- [52] S. Wang, E. Fontana, M. Cerezo, K. Sharma, A. Sone, L. Cincio, and P. J. Coles, *Nat. Commun.* **12**, 6961 (2021).
- [53] K. Bharti, A. Cervera-Lierta, T. H. Kyaw, T. Haug, S. Alperin-Lea, A. Anand, M. Degroote, H. Heimonen, J. S. Kottmann, T. Menke *et al.*, *Rev. Mod. Phys.* **94**, 015004 (2022).
- [54] J. Tilly, H. Chen, S. Cao, D. Picozzi, K. Setia, Y. Li, E. Grant, L. Wossnig, I. Rungger, G. H. Booth, and J. Tennyson, *Phys. Rep.* **986**, 1 (2022).
- [55] S. McArdle, S. Endo, A. Aspuru-Guzik, S. C. Benjamin, and X. Yuan, *Rev. Mod. Phys.* **92**, 015003 (2020).
- [56] Y. I. Bogdanov, A. Y. Chernyavskiy, A. Holevo, V. Lukichev, and A. Orlikovsky, in *Proceedings of the International Conference Micro- and Nano-Electronics 2012* (International Society for Optics and Photonics, Bellingham, 2013), Vol. 8700, p. 87001A.
- [57] E. Paladino, Y. M. Galperin, G. Falci, and B. L. Altshuler, *Rev. Mod. Phys.* **86**, 361 (2014).